Journal of ELECTRONIC MATERIALS, Vol. 50, No. 4, 2021
https://doi.org/10.1007/s11664-020-08699-2

BRIEF COMMUNICATION

Magnetic Ni-Doped TiO_2 Photocatalysts for Disinfection of *Escherichia coli* Bacteria

KHANG CAO NGUYEN,[1,7] NGHIA MANH NGUYEN,[1] VAN QUOC DUONG,[1] KHANH VAN NGUYEN,[1] HUNG MANH NGUYEN,[2] THANG VIET DAO,[2] QUANG VAN NGUYEN,[3] DUC ANH NGUYEN,[3] HA THI VU,[4] CHIEN TRAN DANG,[5,8] and HONG NGOC PHAN[6]

1.—Faculty of Physics, Hanoi National University of Education, 136 Xuan Thuy, Cau Giay, Hanoi, Vietnam. 2.—Hanoi University of Mining and Geology, Co Nhue, North Tu Liem, Hanoi, Vietnam. 3.—Department of Physics and Energy Harvest Storage Research Center, University of Ulsan, Ulsan 44610, Republic of Korea. 4.—University of Transport and Technology, 54 Trieu Khuc, Thanh Xuan, Hanoi, Vietnam. 5.—Hanoi University of Natural Resources and Environment, 41A Phu Dien, North Tu Liem, Hanoi, Vietnam. 6.—Center for High Technology Development Center, Vietnam Academy of Science and Technology, 18 Hoang Quoc Viet, Cau Giay, Hanoi, Vietnam. 7.—e-mail: khangnc@hnue.edu.vn. 8.—e-mail: dtchien@hunre.edu.vn

Ni-doped TiO_2 nanoparticles have been synthesized by a modified sol–gel method. The crystal phase composition, particle size, and magnetic and optical properties of the samples were comprehensively examined using x-ray diffraction analysis, transmission electron microscopy, Brunauer–Emmett–Teller surface area analysis, Raman spectroscopy, magnetization measurements, and ultraviolet–visible (UV–Vis) absorption techniques. The results showed that the prepared Ni-doped TiO_2 samples sintered at 400°C crystallized completely in anatase phase with average particle size in the range from 8 nm to 10 nm and presented broad visible absorption. The bactericidal efficiency of TiO_2 was effectively enhanced by Ni doping, with an optimum Ni doping concentration of 6% (x = 0.06), at which 95% of *Escherichia coli* were killed after just 90 min of irradiation. Density functional theory (DFT) calculations revealed good agreement with the experimental data. Moreover, the Ni dopant induced magnetic properties in TiO_2, facilitating its retrieval using a magnetic field after use, which is an important feature for photocatalytic applications.

Key words: TiO_2, Ni-doped, photocatalytic, *E. coli*

INTRODUCTION

TiO_2 nanostructures have attracted significant interest due to their potential for self-cleaning surfaces, air and water purification systems, photovoltaic sensors, sterilization, and hydrogen evolution.[1–4] Research on photocatalysis by TiO_2 was initiated and promoted in 1972 with the discovery of splitting of water on TiO_2 electrodes using ultraviolet light by Honda.[5] Important features that make TiO_2 so important are its chemical stability, nontoxicity, and low cost.[6–9] However, highly efficient usage of TiO_2 in photocatalytic applications is prevented by its wide bandgap (3.2 eV), which means it responds to only a small fraction of the solar energy spectrum. One of the best ways to improve the performance of TiO_2 is thus to increase its optical activity by shifting the onset of its response from the ultraviolet (UV) to visible region.[10–12]

Attempts to improve the photocatalytic efficiency of TiO_2 have primarily considered the effect of dopants.[13,14] Metal doping and nonmetal doping are

(Received April 5, 2020; accepted December 11, 2020; published online January 25, 2021)

still two main methods to enhance the photocatalytic efficiency of TiO_2.[15–17] Doping a new element into TiO_2 may change the electron density of states, thereby reducing the bandgap. Additionally, doping of transition metals into TiO_2 can induce magnetic properties in this material, facilitating its collection by a magnetic field after use in photocatalytic applications. Umebayashi et al.[18] showed that an electron occupied level is formed in the electronic structure when TiO_2 is doped with Ni, Co, and Mn. Choi et al.[19] reported that Fe-, V-, and Mo-doped TiO_2 showed an increased photoactivity for degradation of $CHCl_3$ under UV irradiation compared with undoped TiO_2. Lai et al.[20] also showed that Ni-doped TiO_2 exhibits higher photoactivity than undoped TiO_2 under UV irradiation. Although many experimental results as well as different theoretical models have been reported to analyze these phenomena in doped TiO_2, the results are not uniform, and some studies even show conflicting results regarding the effects of doping on the visible-light photoactivity. Moreover, the photocatalytic efficiency reported for doped TiO_2 materials may be affected by the specific preparation methods applied, thus the actual photolysis and experimental conditions must be considered to quantify its activity. Unsolved problems remain regarding metal- or nonmetal-doped TiO_2, including the recombination of electron–hole pairs, the formation of clusters of the metal oxide dopant, the mechanisms underlying the optical and photocatalytic properties of doped TiO_2 materials, and the optimum concentration of dopants for each photocatalytic reaction.

The main purpose of this study is to enhance the optical properties of TiO_2 in the visible-light region and to induce magnetic properties in this material to enable its easy retrieval after use. The synthesized Ni-doped TiO_2 was tested for disinfection of *Escherichia coli* bacteria to determine the optimum Ni doping concentration for bactericidal applications. Various techniques such as transmission electron microscopy (TEM), x-ray diffraction (XRD) analysis, Brunauer–Emmett–Teller (BET) surface area analysis, Raman spectroscopy, and UV–Vis spectroscopy were used to understand the surface physical and chemical properties of the samples. The experimental results were combined with density functional theory (DFT) calculations to clarify the origin of the optical and magnetic properties of the Ni-doped TiO_2 materials.

EXPERIMENTAL PROCEDURES

$Ti_{1-x}Ni_xO_2$ (x = 0.00, 0.03, 0.06, and 0.09) powders were prepared via a modified sol–gel method.[21] Firstly, titanium isopropoxide (TTIP) was dissolved in ethanol, followed by stirring for 15 min at 2°C. Then, distilled water was added slowly to the solution under stirring for 30 min. To dope Ni into TiO_2, $Ni(NO_3)_2{\cdot}6H_20$ solution was added to the colloidal nanoparticle solution with molar percentage of Ni doping of 3%, 6%, or 9%. Thereafter, the solution was dried at 180°C for 24 h before being calcined at 400°C for 2 h. Finally, the synthesized powder was crushed in a mortar agate for 10 min before being used as a photocatalyst.

The morphology of the samples was observed by high-resolution (HR)-TEM (F30; Tecnai) at 300 kV and BET measurements (3FLex; Micromeritics). The structure of the TiO_2 samples was characterized by XRD analysis (D5005; Siemens) with Cu K_α radiation (λ = 1.514 Å). Optical absorption spectra were measured by Raman spectroscopy and a V-670 spectrophotometer. Curves of the magnetization as a function of the magnetic field were measured by using a VSM 7300 (Lake Shore). Moreover, theoretical DFT calculations were carried out to obtain the electronic band structure and density of states of the doped materials.

The photocatalytic activity of the samples was evaluated by measuring the disinfection of *E. coli* bacteria under visible-light irradiation from a 100-W incandescent lamp with a 420-nm cutoff filter. First, 10 mg photocatalyst was mixed with 19 ml 0.9% saline solution, then stirred for 1 h. Then, an *E. coli* concentration of approximately 10^7 colony-forming units (CFU)/mL, evaluated by observing the optical density at 600 nm using a UV–Vis spectrophotometer, was added. Before turning on the light, the suspension containing *E. coli* and photocatalyst was magnetically stirred continuously in the dark until no change in absorbance was observed. The purpose of this process is to ensure that the physical adsorption and the disinfection of *E. coli* by the catalyst in the dark were saturated. After turning on the light, the solution was taken out after every 15 min and the number of *E. coli* was counted. A series of tenfold dilutions were performed, and 50 μl of each dilution was plated on nutrient agar. The nutrient agar plates were incubated at 37°C for 48 h before counting was conducted. Additionally, an *E. coli* solution without catalyst was illuminated as a control sample under the same condition to investigate the decomposition of *E. coli* by the light source. The processing of *E. coli* is summarized in Fig. 1.

RESULTS AND DISCUSSION

TEM images of the $Ti_{1-x}Ni_xO_2$ (x = 0.00, 0.03, 0.06, and 0.09) powders synthesized by the modified sol–gel method are presented in Fig. 2, revealing that the samples contained mainly homogeneous and well-dispersed spherical particles. The powder particles of pure TiO_2 had a size of 10 nm, while the size of the $Ti_{1-x}Ni_xO_2$ (x = 0.03, 0.06, and 0.09) particles was determined to be 8 nm, a relatively small change that prevents any definitive conclusions regarding the dependence of the particle size on the Ni doping concentration.

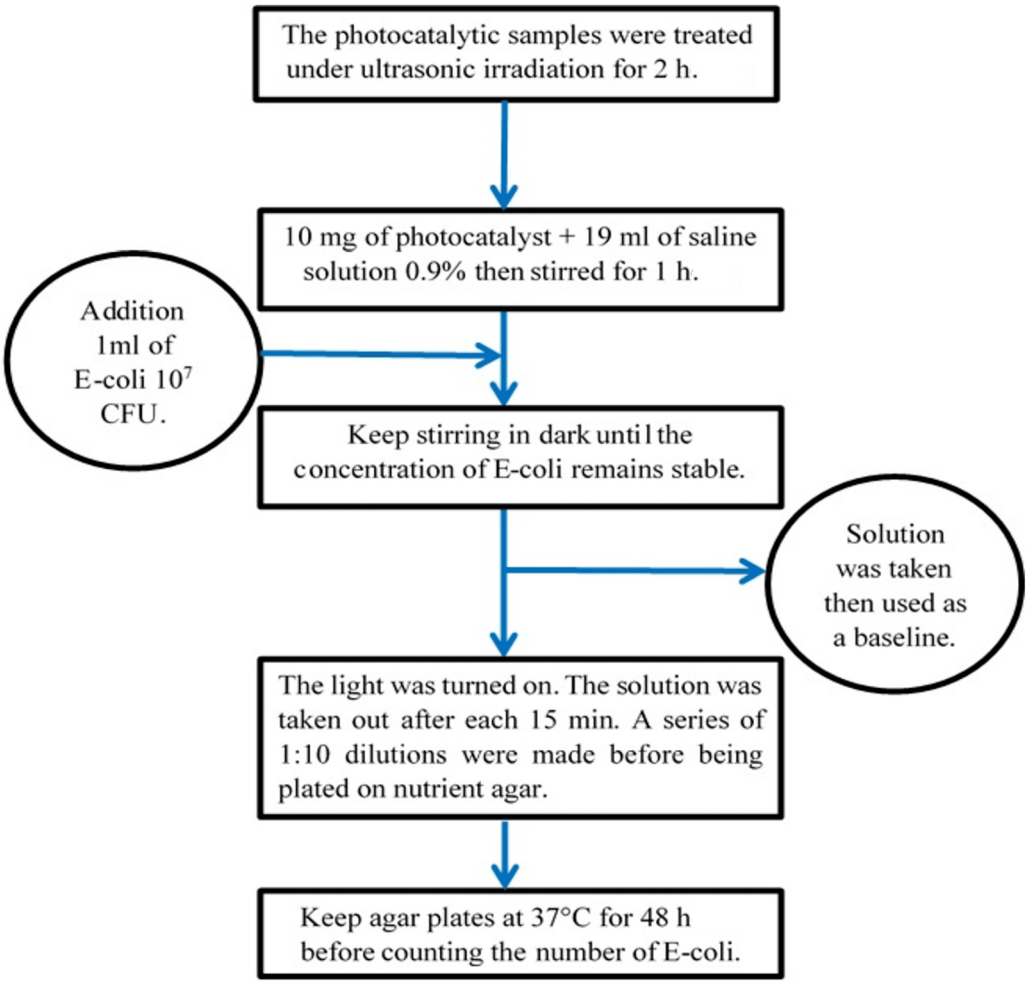

Fig. 1. Schematic diagram of *E. coli* bacterial disinfection.

The results of the surface area measurements on the $Ti_{1-x}Ni_xO_2$ (x = 0.00, 0.03, 0.06, and 0.09) samples using the BET method are shown in Fig. 3. All the $Ti_{1-x}Ni_xO_2$ powders displayed type IV isotherms (known to be characteristic of mesoporous texture) with an H3 hysteresis loop, which is commonly found in medium capillary materials with average size range from 1 nm to 10 nm. The surface area of the pure TiO_2 was determined to be 31.6 m^2/g. Upon doping with 3%, 6%, and 9% Ni, the surface area value increased to 35.7 m^2/g, 35.4 m^2/g, and 38.2 m^2/g, respectively. This increase in the surface area of TiO_2 will increase the number of active sites, further reducing the electron–hole pair recombination and thereby enhancing the photocatalytic activity. These results imply that Ni doping effectively inhibited the growth of TiO_2 grains, leading to a decrease of the particle size and an increase of the surface area.[22,23]

The crystal structure of the samples was determined by x-ray diffraction analysis. Figure 4 shows the XRD patterns of the $Ti_{1-x}Ni_xO_2$ (x = 0.00, 0.03, 0.06, and 0.09) powders. The peaks at 2θ angles of 25.5°, 37.8°, 48.1°, 53.8°, 54.7°, and 62.8°, corresponding to (101), (004), (200), (105), (211), and (204) planes, respectively, are all characteristic of anatase phase. On the other hand, no secondary phase was observed, suggesting that Ni^{2+} ions may enter the anatase phase and substitute at Ti^{4+} sites. However, the possible existence of Ni oxide clusters, which are not detectable by the XRD technique, cannot be ruled out. The shoulder next to (101) peak corresponds to (110) plane of rutile phase. In the Ni-doped TiO_2 samples, the Ni^{2+} will increase the number of oxygen vacancies in the TiO_2 crystal structure. These oxygen vacancies are responsible for the enhancement of the transformation from the anatase to rutile phase.

Figure 5 shows the Raman spectra of the $Ti_{1-x}Ni_xO_2$ powder samples. For the body-centered tetragonal anatase structure, the frequencies of six Raman-active modes ($3E_g + 2B_{1g} + A_{1g}$) were predicted by group theory and confirmed experimentally by Ohsake et al.[24] Among those, the E_g peaks are mainly due to symmetric stretching vibration, the B_{1g} peaks result from symmetric bending vibration, while the A_{1g} peak corresponds to antisymmetric bending vibration of O–Ti–O. The

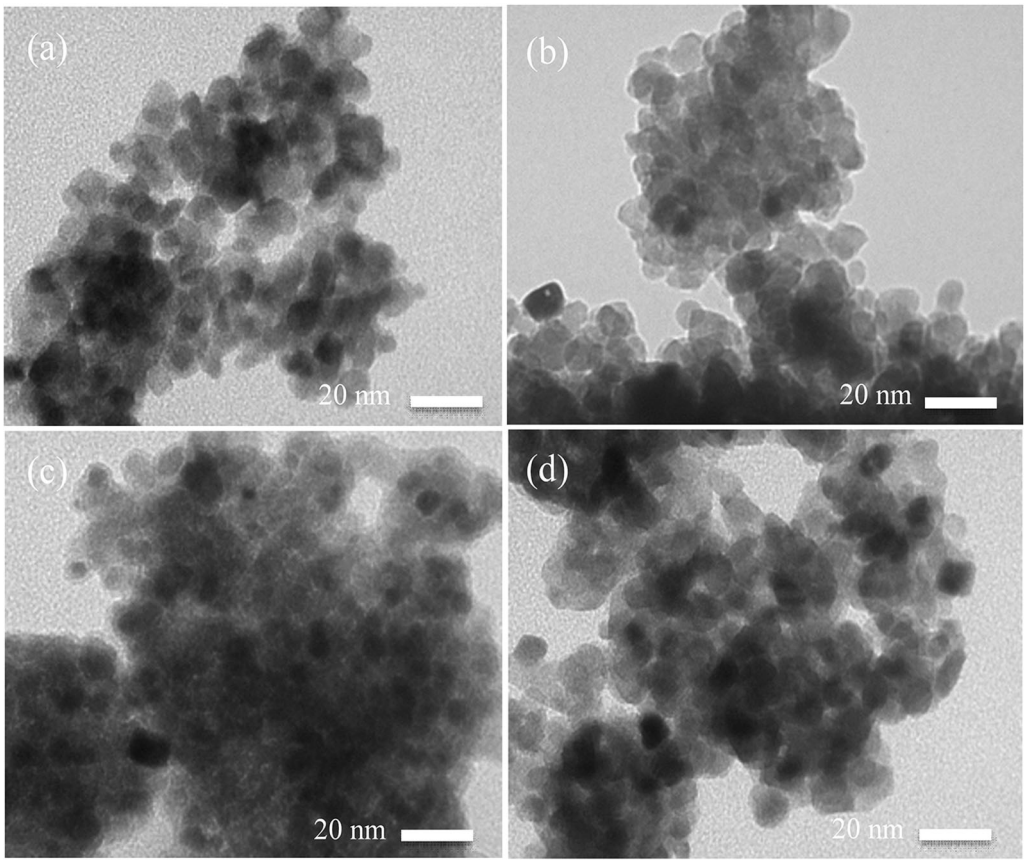

Fig. 2. TEM images of $Ti_{1-x}Ni_xO_2$ with (a) $x = 0.00$, (b) $x = 0.03$, (c) $x = 0.06$, and (d) $x = 0.09$.

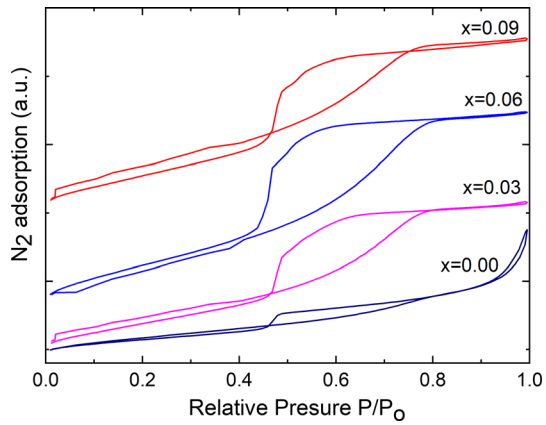

Fig. 3. N_2 adsorption–desorption isotherms for $Ti_{1-x}Ni_xO_2$ samples.

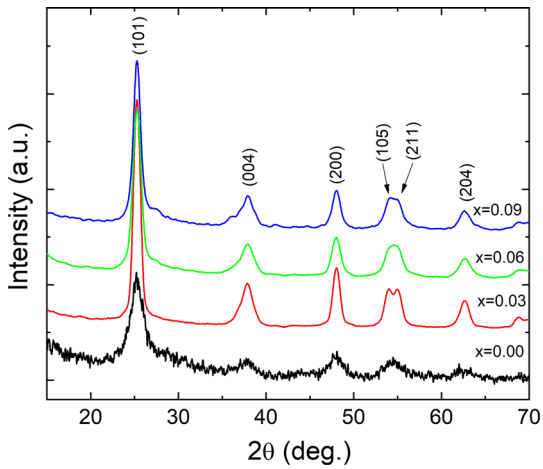

Fig. 4. X-ray diffraction patterns of $Ti_{1-x}Ni_xO_2$ samples.

frequencies and relative intensities of three Raman peaks, observed in Fig. 5, are well comparable to the values reported for the B_{1g} (399 cm^{-1}), A_{1g} (513 cm^{-1}) (whose frequency is close to that of the B_{1g} mode at 519 cm^{-1}), and E_g (637 cm^{-1}) modes of anatase TiO_2. No impurity-related modes were observed, consistent with the XRD results described above. Since Raman spectroscopy is much more phase sensitive than XRD analysis, this observation allows us to conclude that Ni^{2+} ions entered the anatase phase and substituted at Ti^{4+} sites in our Ni-doped TiO_2 samples.

It is also noted that the bands at 512 cm^{-1} to 519 cm^{-1}, corresponding to the A_{1g} mode of our samples, shifted a few cm^{-1} towards lower wavenumber as the Ni doping concentration was increased. This phenomenon is related to phonon confinement and surface stress effects,[25,26] usually being observed for materials with particle size below 10 nm. According to this model, when the particle

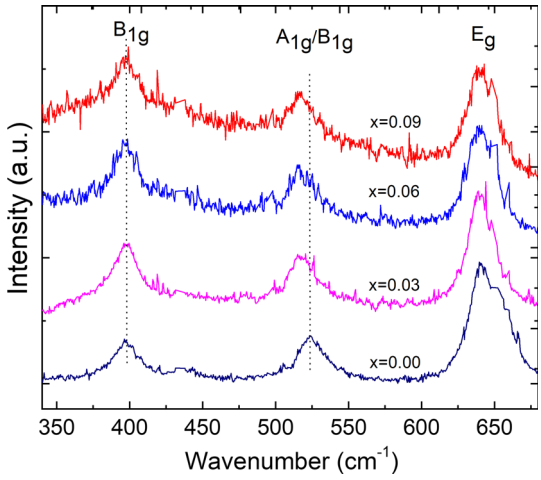

Fig. 5. Raman spectra of $Ti_{1-x}Ni_xO_2$ samples.

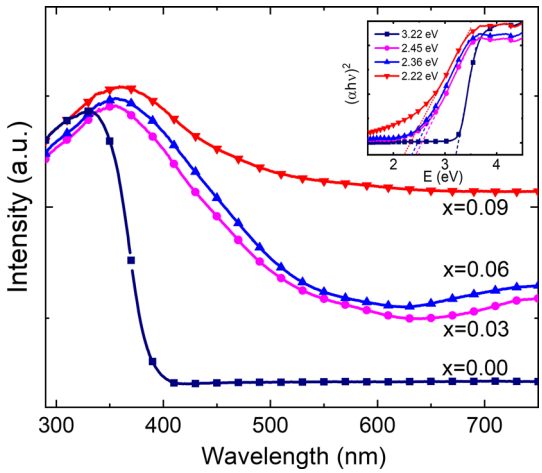

Fig. 6. UV–Vis diffuse reflectance spectra of $Ti_{1-x}Ni_xO_2$ samples.

size decreases to the nanometer scale, the vibrational properties can be strongly affected by the change in crystal size. In contrast, the B_{1g} and E_g bands exhibit no similar shift. This finding is different from our previous experiments, where doping caused a red- or blue-shift of all Raman modes.[27] This may be due to the fact that the change in the force constant is insignificant for the symmetric bending B_{1g} and symmetric stretching E_g modes, although it is important for the antisymmetric A_{1g} mode. On the other hand, we observe asymmetrical profiles for the A_{1g} and E_g bands (Fig. 5), while the B_{1g} band appears to be symmetric in the Raman spectra of our samples. It has been reported that the phonon confinement effect is one possible reason for an asymmetric shape of the Raman peaks. Furthermore, according to the Heisenberg uncertainty principle, a decrease in the particle size will also lead to asymmetrical broadening.

Figure 6 shows the UV–Vis spectra of our $Ti_{1-x}Ni_xO_2$ (x = 0.00, 0.03, 0.06, and 0.09) samples. As

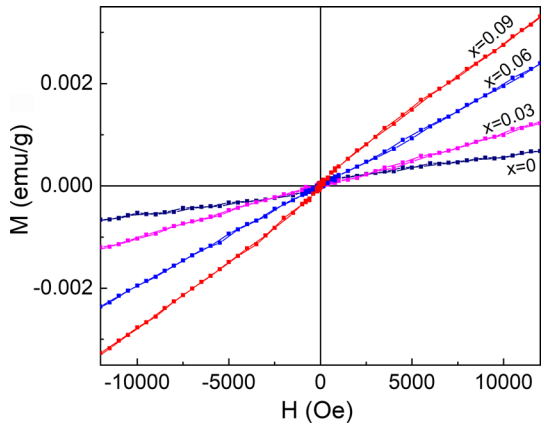

Fig. 7. $M(H)$ curves of $Ti_{1-x}Ni_xO_2$ samples.

the Ni doping concentration was increased from 1% to 9%, both the absorption peak and absorption edge shifted to longer wavelength. While undoped TiO_2 only absorbed ultraviolet light (under 400 nm), all the Ni-doped TiO_2 samples could strongly absorb visible light (400 nm to 700 nm). This result reconfirms the replacement of Ti by Ni in the lattice of our Ni-doped samples. It is also noted that the visible-light absorbance of the samples increased with their Ni content. The direct bandgap (E_g) of the samples can be estimated by fitting the absorption data to the direct transition equation,

$$\alpha h\vartheta = E_d\left(h\vartheta - E_g\right)^{1/2}, \quad (1)$$

where α is the optical absorption coefficient, $h\vartheta$ is the photon energy, E_g is the direct bandgap, and E_d is a constant. $(\alpha h\vartheta)^2$ is linearly dependent on $(h\vartheta - E_g)$, and a plot of $(\alpha h\vartheta)^2$ versus photon energy offers an easy way to determine the optical bandgap of the material. The optical bandgap calculated for our samples decreased from 2.45 eV to 2.22 eV as the Ni doping concentration was increased from 3% to 9%. This narrowing of the optical bandgap also provides evidence of the presence of Ni in the host lattice.

Vibrating-sample magnetometry (VSM) was used to measure the magnetic properties of the samples. Figure 7 shows the room-temperature magnetization curves for all the samples. The linear dependence of the magnetization on the applied magnetic field indicates a paramagnetic characteristic for our samples. This observation is a consequence of the nanosize of the particles in our samples, mentioned above. As seen from this figure, the magnetization increases with the Ni content. This observation can be easily understood as due to the fact that the ferromagnetism in Ni-doped TiO_2 is mediated by a superexchange d–d interaction that increases with the Ni doping concentration, leading to an increase in the magnetization of the samples.

The effects of Ni doping on the physical properties of TiO_2 were further studied theoretically using

DFT calculations. All the calculations are based on the Perdew–Burke–Ernzerhof method with a unit cell of size $2 \times 2 \times 2$ consisting of 16 titanium atoms and 13 oxygen atoms. By replacing one Ti atom of the TiO_2 lattice by a Ni atom, the structure of the $Ti_{1-x}Ni_xO_2$ ($x = 0.0625$) sample is formed. Figure 8a shows the density of states of 6.25% Ni-doped TiO_2, revealing the formating of a new band near the Fermi level. The localized band originates from the Ni 3*d* orbitals, as shown in Fig. 8b. The presence of Ni changes the density of states of O and Ti, leading to the change in the total density of states. As seen from the electronic band structure of Ni-doped TiO_2 (Fig. 8c, left), a dopant energy level appears inside the bandgap, close to the valence band. This additional energy level causes the narrowing of the optical bandgap of TiO_2, which is consistent with the UV–Vis data.

Photodecomposition of *E. coli* in solution was carried out under visible light. The catalyst was added to 10^7 CFU *E. coli* solution. The solution was taken out every 15 min and diluted several times before transferring to agar plates. Figure 9 shows the *E. coli* decomposition as a function of the irradiation time for all the samples under dark and visible-light irradiation conditions. As seen from this figure, all the samples showed weak bactericidal ability in the dark but good bactericidal ability under visible-light irradiation. For pure TiO_2, after 60 min in the dark, the concentration of *E. coli* had decreased by only about 3%. This decrease is mainly due to *E. coli* bacteria attaching to the catalyst surface. However, for the 3%, 6%, and 9% Ni-doped TiO_2, the concentration of *E. coli* decreased to 8%, 10%, and 13%, respectively. This decrease occurred as soon as the catalyst was added to the *E. coli* solution and reached saturation after 30 min. Under visible-light irradiation, the bactericidal efficiency of all the samples rapidly increased with the irradiation time, especially for the Ni-doped samples. At 15 min of irradiation, about 25% of the *E. coli* had disintegrated, while by the end of the irradiation process, i.e., at 90 min, more than 85% of the *E. coli* had disintegrated. On the other hand, the bactericidal efficiency under irradiation increased rapidly with the Ni content, reaching a maximum value for $x = 0.06$, then decreasing slightly at $x = 0.09$. The bactericidal efficiency of the Ni-doped TiO_2 was about four to five times greater than that of pure TiO_2. These results indicate that the optimum Ni doping concentration to improve the bactericidal ability of TiO_2 is about 6% ($x = 0.06$), for which 95% of *E. coli* were killed after just 90 min of irradiation. The results also highlight the superiority of Ni-doped TiO_2 compared with pure TiO_2, in terms of its bactericidal effect on *E. coli* under visible-light irradiation. Attempts have been made to determine the reasons for the enhanced bactericidal efficiency of doped catalysts.[28–30] In some cases, metal-doped catalysts

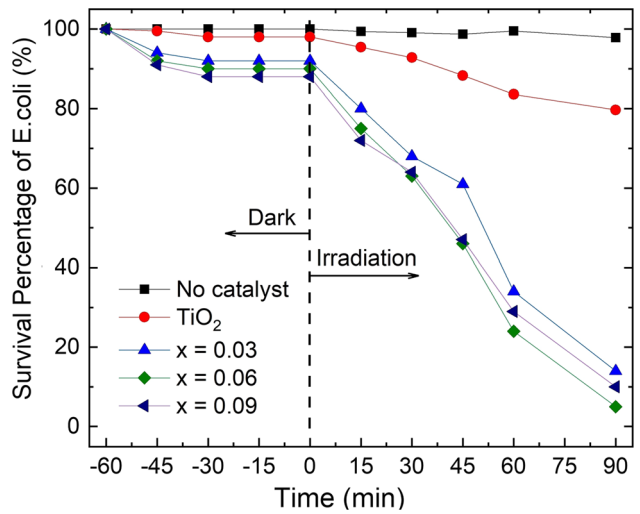

Fig. 9. Photodecomposition of *E. coli* catalyzed by the catalysts under visible-light illumination.

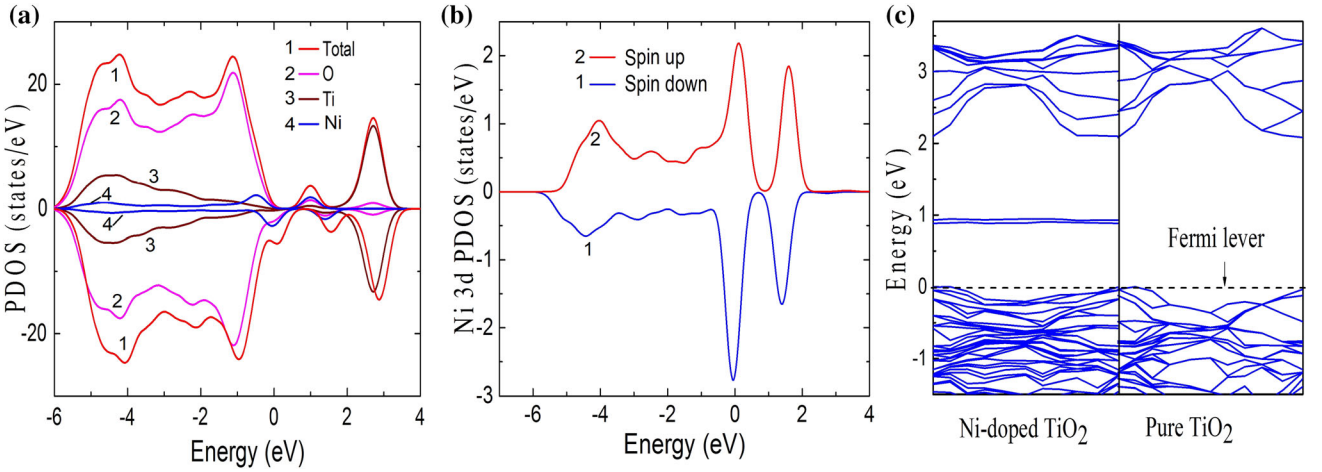

Fig. 8. (a) Density of states (DOS) of 6.25% Ni-doped TiO_2 and (b) spin state of Ni 3*d* in 6.25% Ni-doped TiO_2. (c) Band structure of Ni-doped TiO_2 (left) and pure TiO_2 (right).

can induce destruction of bacterial cells due to the toxicity of metal ions released into the reaction solution. In this study, a high concentration of Ni doping can be considered to be one of the reasons for the enhanced *E. coli* bactericidal efficiency. It is clear that the high concentration of Ni doped into TiO_2 catalyst is toxic to *E. coli* bacteria, considering their short-term toxic effects. At high concentration, redox-active metal ions are very toxic.[31] The second cause of the increase in the photocatalytic efficiency is the shift of the absorption of the catalysts to the visible region up to 600 nm, as well as the decrease of the bandgap energy, as clearly shown in Fig. 6. Moreover, dopants located on the surface of TiO_2 may act as electron traps, thus promoting interfacial charge transfer and delaying the recombination of electron–hole pairs,[32] which also leads to an activity enhancement.

CONCLUSIONS

$Ti_{1-x}Ni_xO_2$ (x = 0, 0.03, 0.06, and 0.09) photocatalysts were successfully prepared by a modified sol–gel method. The Ni-doped TiO_2 crystallized in anatase phase with particle size ranging from 8 nm to 10 nm. The substitution of Ni^{2+} ions at Ti^{4+} sites in the TiO_2 crystal resulted in a shift of the Raman peaks. We observed a shift of the absorption edge towards longer wavelength and an increase of the absorbance with Ni doping content. DFT calculations showed good agreement with the experimental data. The bactericidal efficiency of TiO_2 was effectively enhanced by Ni doping. The optimum Ni doping concentration to improve the bactericidal ability of TiO_2 was found to be 6% (x = 0.06), for which 95% of *E. coli* were killed after just 90 min of irradiation.

ACKNOWLEDGMENT

This work was supported by Nafosted No. 103.02-2016.66.

CONFLICT OF INTEREST

The authors declare that they have no conflicts of interest.

REFERENCES

1. X. Chen and S.S. Mao, *Chem. Rev.* 107, 2891 (2007).
2. M.J. Sailor and J.H. Park, *Adv. Mater.* 24, 3779 (2012).
3. C. Li and W.D. Wang, *Chin. J. Chem. Phys.* 22, 423 (2009).
4. S.S. Lin, Y.H. Hung, and S.C. Chen, *Thin Solid Films* 517, 4621 (2009).
5. A. Fujishima and K. Honda, *Nature* 238, 37 (1972).
6. X. Li, R. Xiong, and G. Wei, *J. Hazard. Mater.* 164, 587 (2009).
7. U. Diebold, *Surf. Sci. Rep.* 48, 53 (2003).
8. M. Li, P. Tang, Z. Hong, and M. Wang, *Colloid Surface A Physicochem. Eng. Asp.* 318, 285 (2008).
9. M. Li, Z. Hong, Y. Fang, and F. Huang, *Mater. Res. Bull.* 43, 2179 (2008).
10. N.C. Khang, N.V. Minh, and I.S. Yang, *J. Nanosci. Nanotechnol.* 11, 1 (2011).
11. M. Shen, Z. Wu, H. Huang, Y. Du, Z. Zou, and P. Yang, *Mater. Lett.* 60, 693 (2006).
12. H. Sun, G. Zhou, S. Liu, H.M. Ang, M.O. Tade, and S. Wang, *Chem. Eng. J.* 231, 18 (2013).
13. Y. Wang, Y. Meng, Y. Ding, H. Shan, Y. Zhao, and X. Tang, *J. Phys. Chem. C* 112, 6620 (2008).
14. R. Asahi, T. Morikawa, T. Ohwaki, K. Aoki, and Y. Taga, *Science* 293, 269 (2001).
15. H. Luo, T. Takata, Y. Lee, J. Zhao, and K. Domen, *Chem. Mater.* 16, 846 (2004).
16. N.C. Khang, D.Q. Van, N.M. Thuy, N.V. Minh, and P.N. Minh, *J. Phys. Chem. Solids* 99, 119 (2016).
17. K. Nagaveni, M.S. Hegde, and G. Madras, *J. Phys. Chem. B* 108, 20204 (2004).
18. T. Umebayashi, T. Yamaki, H. Itoh, and K. Asai, *J. Phys. Chem. Solids* 63, 1909 (2002).
19. W. Choi, A. Termin, and M.R. Hoffmann, *J. Phys. Chem.* 98, 13669 (1994).
20. L.L. Lai, W. Wen, and J.M. Wu, *RSC Adv.* 6, 25511 (2016).
21. L.L. Hench and J.K. West, *Chem. Rev.* 90, 33 (1990).
22. L.G. Devi, N. Kottam, S.G. Kumar, and K.E. Rajashekhar, *Cent. Eur. J. Chem.* 8, 142 (2010).
23. X. Shu, J. He, and D. Chen, *Ind. Eng. Chem. Res.* 47, 4750 (2008).
24. T. Ohsaka, F. Izumi, and Y. Fujiki, *J. Raman Spectrosc.* 7, 321 (1978).
25. C. Lejon and L. Österlund, *J. Raman Spectrosc.* 42, 2026 (2011).
26. S. Kelly, F.H. Pollak, and M. Tomkiewicz, *J. Phys. Chem. B* 101, 2730 (1997).
27. N.V. Minh, N.T.M. Hien, V. Vien, S.J. Kim, W.S. Noh, I.S. Yang, D.T. Dung, N.C. Khang, and N.T. Khoi, *J. Korean Phys. Soc.* 52, 1629 (2008).
28. D. Venieri, A. Fraggedaki, M. Kostadima, E. Chatzisymeon, V. Binas, A. Zachopoulos, G. Kiriakidis, and D. Mantzavinos, *Appl. Catal. B Environ.* 154–155, 93 (2014).
29. V. Bhatia and A. Dhir, *J. Environ. Chem. Eng.* 4, 1267 (2016).
30. M.P. Reddy, A. Venugopal, and M. Subrahmanyam, *Water Res.* 41, 379 (2007).
31. C. Ranquet, S. Ollagnier-de-Choudens, L. Loiseau, F. Barras, and M. Fontecave, *J. Biol. Chem.* 282, 30442 (2007).
32. W. Wang, J. Zhang, F. Chen, D. He, and M. Anpo, *J. Colloid Interface Sci.* 323, 182 (2008).